The Astrophysical Journal, 1010:93 (13pp), 2026 October 10 https://doi.org/10.3847/1538-4357/aea6dd
© 2026. The Author(s). Published by the American Astronomical Society.
OPEN ACCESS

Radial Evolution of Turbulent Modes near the Sun Using Parker Solar Probe and Solar Orbiter Measurements

Monika Karki[1,2], Gary P. Zank[1,2], B. L. Alterman[3], and Laxman Adhikari[1,2]
[1] Department of Space Science, University of Alabama in Huntsville, Huntsville, AL 35899, USA
[2] Center for Space Plasma and Aeronomic Research, University of Alabama in Huntsville, Huntsville, AL 35899, USA
[3] Heliophysics Laboratory, NASA Goddard Space Flight Center, Greenbelt, MD 20771, USA
Received 2026 August 14; revised 2026 September 8; accepted 2026 September 11; published 2026 October 9

Abstract

We investigate the radial evolution of turbulent fluctuations in the inner heliosphere using Parker Solar Probe and Solar Orbiter observations over heliocentric distances of ∼32–90 $R_{\odot}$. We decompose the measured fluctuations of density, velocity, and magnetic field into eight fundamental magnetohydrodynamic modes using the linear mode decomposition technique. The mode-resolved energy results show that the fluctuation energy is highly field-dependent: Velocity fluctuations are primarily Alfvénic, with both forward and backward Alfvén modes exhibiting relatively shallow radial decay, whereas magnetic fluctuations are dominated by transverse nonpropagating incompressible / magnetic island–like components. In particular, the magnetic island mode decreases approximately as $\delta B^{i} \sim r^{-1.90}$, followed closely by the forward and backward Alfvénic magnetic modes, $\delta B^{\mathrm{A}+} \sim r^{-1.96}$ and $\delta B^{\mathrm{A}-} \sim r^{-2.17}$. In contrast, density fluctuations are mainly governed by fast magnetosonic modes, while entropy and slow magnetosonic contributions remain comparatively weaker and decay more rapidly with heliocentric distance. We find that the variance anisotropy of the transverse incompressible magnetic island mode (δB^{i}) and the Alfvén modes ($\delta B^{\mathrm{A}\pm}$) increases slightly with heliocentric distance. These results will help identify which magnetohydrodynamic modes are responsible for carrying turbulent energy in the inner heliosphere and how that energy evolves with distance from the Sun.

Unified Astronomy Thesaurus concepts: Interplanetary turbulence (830); Solar wind (1534); Magnetohydrodynamics (1964)

1. Introduction

Turbulence is a fundamental process in the heliosphere that controls the transport of energy, the heating and acceleration of the solar wind, and the scattering of energetic particles and cosmic rays (H. Yan & A. Lazarian 2004; G. Zank et al. 2011; R. Bruno & V. Carbone 2013; G. P. Zank et al. 2017; L. Adhikari et al. 2020b, 2024; A. Silwal et al. 2024). Direct, in situ observations of the solar wind near 1 au (E. Marsch & C.-Y. Tu 1990; A. Balogh et al. 1992; C.-Y. Tu & E. Marsch 1994) and studies using the Parker Solar Probe (PSP) inward to ∼0.29 au have explored magnetohydrodynamic (MHD) wave turbulence and its modal composition, but their relative importance is expected to change closer to the Sun (C.-Y. Tu & E. Marsch 1995; S. Yao et al. 2011; G. Howes et al. 2012; G. P. Zank et al. 2024).

The drivers of in situ solar wind energization remain constrained by both theory (W. H. Matthaeus et al. 1999; G. P. Zank et al. 2012, 2017) and observations (R. Bruno & V. Carbone 2013; R. Bandyopadhyay et al. 2020; C. C. Chaston et al. 2020; C. H. K. Chen et al. 2020). In the context of MHD, one key driver is the turbulent cascade, in which energy flows from larger MHD to smaller scales (L. Adhikari et al. 2021, 2022, 2025; G. Zank et al. 2021) and, at scales comparable to ions/electrons (C. H. K. Chen et al. 2020), this energy dissipates, and solar wind charged particles are heated. Broadly, MHD turbulence in the solar wind can be classified by its Alfvénicity and compressibility. These two properties can produce distinct solar wind energization signatures: Alfvénic fluctuations play a crucial role in the MHD turbulent cascade (P. Goldreich & S. Sridhar 1995; S. Boldyrev 2005) because their nonlinear interactions lead to scale-dependent anisotropy with respect to the mean magnetic field $\boldsymbol{B}_0$. Compressive fluctuations directly modify plasma pressure, density, velocity, and magnetic field strength; in compressible MHD, slow magnetosonic (MS) modes are more field-aligned, whereas fast MS modes can propagate efficiently both along and across the magnetic field. Numerical and theoretical investigations by J. Cho & A. Lazarian (2003) and A. Lazarian & J. Cho (2004) demonstrated that Alfvén, slow, and fast modes exhibit distinct cascades with relatively weak coupling, with slow modes largely following the Alfvénic cascade and fast modes developing a more isotropic and independent cascade. In the context of the solar wind, spacecraft observations (R. Bruno & V. Carbone 2013; R. D'Amicis & R. Bruno 2015) have consistently shown that turbulence is predominantly Alfvénic, particularly in the inner heliosphere, but with a significant contribution from compressive fluctuations, whose origin and evolution remain an active area of research. Reviews by R. Bruno & V. Carbone (2013) and C. Chen (2016) further synthesize observational evidence, showing that while Alfvénic fluctuations dominate the inertial range, compressive components, often associated with slow and fast MS modes, play a nonnegligible role in shaping turbulence dynamics and energy distribution. Although Alfvénic fluctuations dominate the nonlinear cascade and outward transport of turbulent energy, they do not fully describe the role of density, pressure, and magnetic field strength fluctuations in energy transfer across scales. It remains unresolved whether compressive fluctuations are passively generated by the Alfvénic cascade, correspond to

Original content from this work may be used under the terms of the Creative Commons Attribution 4.0 licence. Any further distribution of this work must maintain attribution to the author(s) and the title of the work, journal citation and DOI.

distinct slow and fast MS modes, or contribute directly to plasma heating and intermittency. Nearly incompressible MHD theory links such density and pressure fluctuations to an underlying incompressible cascade (G. Zank & W. Matthaeus 1992; G. P. Zank et al. 2017), while PSP observations show that slow- and fast-mode contributions can coexist with dominant Alfvénic turbulence close to the Sun (C. C. Chaston et al. 2020). Building on our previous 1 au study of Alfvénic and compressive properties in different solar wind regimes (M. Karki et al. 2025), this motivates a mode-based analysis of how Alfvén, slow, fast, and nonpropagating fluctuations are organized near the Sun and how their relative contributions evolve with heliocentric distance.

Several studies have examined the radial evolution of solar wind properties during alignments (D. Telloni et al. 2021; A. Silwal et al. 2025), with recent results suggesting that Alfvén waves may preferentially heat and accelerate fast solar wind streams. Observational and theoretical studies by W. H. Matthaeus et al. (1990) and G. Zank & W. Matthaeus (1992), along with turbulence transport models developed by G. P. Zank et al. (2017) and G. Zank et al. (2020), have provided a comprehensive description of solar wind turbulence consisting of a superposition of Alfvénic fluctuations and quasi-2D structures such as magnetic islands, consistent with nearly incompressible MHD theories. These models predict the radial evolution of turbulence amplitudes, variance anisotropy, and mode composition, highlighting the increasing role of nonlinear interactions and the emergence of coherent structures such as current sheets and magnetic islands with heliocentric distance. Furthermore, as the solar wind expands, nonlinear interactions progressively modify the turbulent cascade, reducing Alfvénicity and increasing the relative contribution of quasi-2D structures and coherent magnetic features. This framework serves as the basis for differentiating between propagating Alfvénic and MS fluctuations and nonpropagating turbulent structures, as well as for evaluating the radial evolution of MHD mode composition.

Recent advances in mode decomposition techniques applied to spacecraft observations have enabled a more direct separation of solar wind fluctuations into distinct propagating MHD modes, allowing their relative contributions and radial evolution (e.g., C. C. Chaston et al. 2020; X. Zhu et al. 2020; L.-L. Zhao et al. 2023; S. Zhao et al. 2026). These studies suggest that the balance between modes evolves with the heliocentric distance, reflecting changes in plasma conditions such as plasma beta, Alfvénicity, and expansion effects. However, these studies generally do not include nonpropagating components, which can also make important contributions to the turbulent energy and compressive variability of the solar wind. These include entropy-related density and pressure fluctuations, which are advected with the solar wind flow and reflect thermodynamic inhomogeneities (P. Hunana & G. Zank 2010; L. Adhikari et al. 2017, 2020a; G. P. Zank et al. 2017), as well as structure-like magnetic fluctuations such as flux ropes and magnetic islands (M. Moldwin et al. 2000; D. Telloni et al. 2013; Y. Chen et al. 2019; L.-L. Zhao et al. 2021). Including these nonpropagating components is essential for a more complete description of solar wind turbulence because they contribute to intermittency, pressure balance, magnetic structuring, and the partition of turbulent energy between propagating waves and advected coherent structures.

Despite these advances, the detailed radial evolution of individual MHD modes, particularly in the near-Sun region, remains incompletely understood. A major challenge in addressing this problem has been the lack of robust techniques to separate these modes observationally, particularly using single-spacecraft measurements. Recent spacecraft missions such as NASA's PSP and ESA's Solar Orbiter (SolO) now provide high-resolution observations of the near-Sun solar wind, enabling the study of turbulence closer to the source region than ever before. However, determining the physical wave modes that comprise the turbulent fluctuations remains difficult since data includes combinations of numerous plasma wave modes. Classical mode decomposition (K. Glassmeier et al. 1995), which uses only the six propagating modes (forward and backward fast/slow MS and Alfvén modes), does not explicitly account for nonpropagating compressive or coherent structures. Linear mode decomposition (LMD) builds on this approach by incorporating both propagating MHD modes and nonpropagating entropy and magnetic island modes, thereby separating plasma and magnetic field fluctuations into a more complete set of fundamental MHD components (G. Zank et al. 2023; G. P. Zank et al. 2024). This method has been applied to several solar wind intervals. This includes different solar wind regimes (M. Karki et al. 2025; P. Baruwal et al. 2026a), shock-associated intervals (S. P. Gautam et al. 2025), and radially aligned spacecraft observations (P. Baruwal et al. 2026b), demonstrating its application for identifying the modal composition of observed turbulent fluctuations and for examining how propagating and nonpropagating modes evolve under different heliospheric conditions. These studies have been limited to near-Earth measurements, where turbulence has already undergone substantial nonlinear evolution. Thus, in this work, we apply LMD to in situ PSP and Solar Orbiter measurements to investigate the radial evolution of plasma wave modes in solar wind turbulence in the inner heliosphere. Specifically, this study seeks to address the following questions: (i) How do the individual linear modes evolve with heliocentric distance in the near-Sun environment? (ii) How does the relative power contribution of each mode change as the solar wind expands away from the Sun? (iii) How does the magnetic field fluctuations' spectral index vary with heliocentric distance? The findings from this investigation will help identify the mode composition and propagation properties of MHD fluctuations in the inner heliosphere, revealing how turbulent energy is organized, transported, and partitioned among plasma modes in the young solar wind. The paper is organized as follows. Section 2 outlines the datasets and methodology. Section 3 presents the main results. Finally, Section 4 discusses the key findings and Section 5 concludes the paper.

2. Data Overview

Figure 1 shows an overview of the solar wind plasma environment during PSP perihelion passages corresponding to encounters 1–19, covering a heliocentric radial distance range of 0.05–0.26 au (or equivalently 11.43–55.95 $R_\odot$). Solar Orbiter measurements covering heliocentric distances from 60 to 90 $R_\odot$ are also shown. We used magnetic field data from the PSP/FIELDS fluxgate magnetometer (MAG) measurements (S. Bale et al. 2016), and plasma parameters measured by the Solar Wind Electrons Alphas and Protons (SWEAP) instrument (J. C. Kasper et al. 2016). The two SWEAP

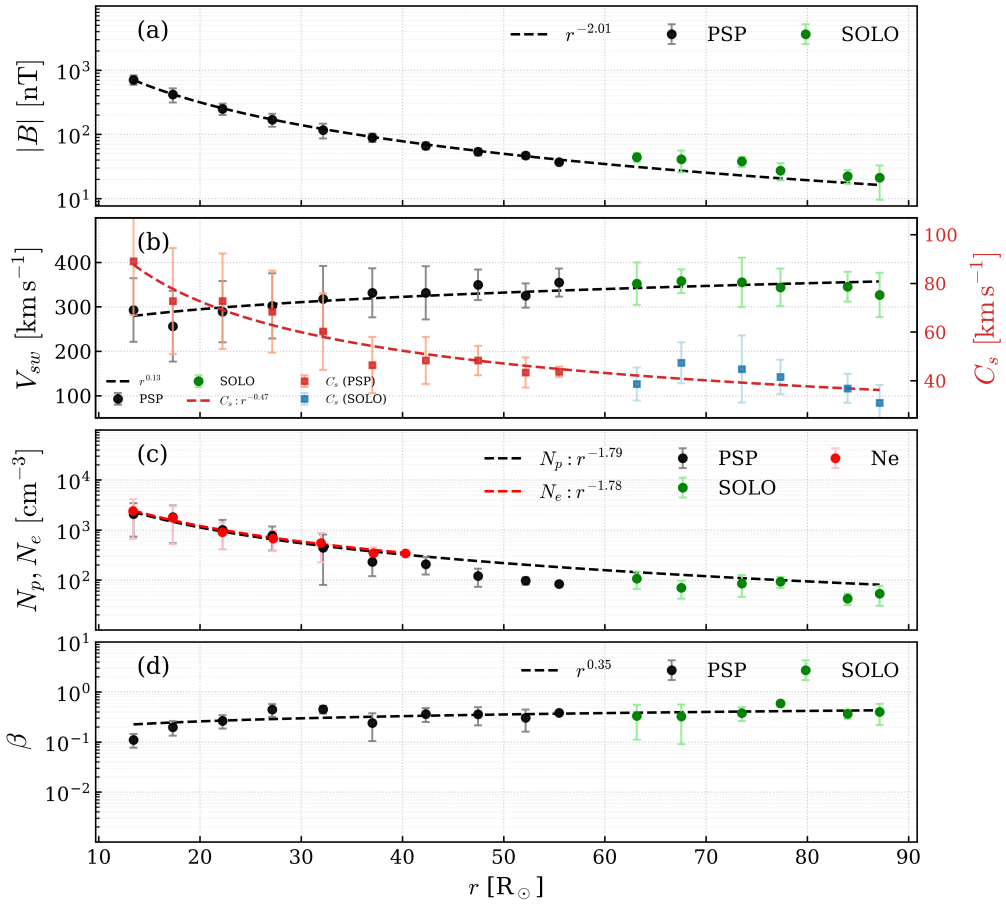


Figure 1. Overview of the field and plasma measurements from PSP and Solar Orbiter over heliocentric distances of approximately 11–90 $R_\odot$. From top to bottom, the panels show the magnetic field magnitude $|B|$, the solar wind speed V together with the sound speed C_s, the proton number density N_p and electron number density N_e, and the plasma beta β. The symbols represent the measured values with error bars, while the dashed curves indicate power-law fits as a function of radial distance r.

sensors, SPC and SPAN-I, provide the ion measurements used for PSP. SPC is a Sun-pointing Faraday cup that is best suited to the early encounters, when the solar wind flow is primarily radial in the spacecraft frame (A. W. Case et al. 2020). SPAN-I is a ram-facing electrostatic analyzer with time-of-flight capability that becomes more effective during later, closer encounters as PSP's increasing orbital speed makes the flow more nonradial (R. Livi et al. 2022). Accordingly, we used SPC ion data for encounters 1–4 and SPAN-I ion data for encounters 5–19. Using these data, we analyzed in situ solar wind time series over ±2 days around each perihelion with a sliding window of 10 minutes at a 3.5 s resolution. We also used Solar Orbiter (SolO) magnetometer data (T. S. Horbury et al. 2020) and Solar Wind Analyser Proton-alpha Sensor (SWA-PAS) plasma data (C. J. Owen et al. 2020) for the selected solar wind intervals analyzed in this study. The MAG measurements provide the vector magnetic field, while SWA-PAS provides the proton bulk velocity, density, and temperature. The selected intervals were chosen to represent slow solar wind streams observed by SolO. The detailed time periods for the selected intervals are listed in Table 1.

To avoid contamination by missing or low-quality data, we required that at least 60% of the data in each 10 minute interval have valid non-NaN ion moments. For the LMD analysis, we identified 133 intervals within the distances from ∼32 to 90 $R_\odot$. To ensure the validity of the LMD, we applied uniform selection criteria to all intervals, retaining only those with plasma beta $\beta < 5$, Alfvén Mach number $1 < M_A < 5$, and bulk solar wind speed $V_{sw} < 450\,\mathrm{km\,s^{-1}}$ (B. Alterman & R. D'Amicis 2025) and thereby ensuring comparison of a broadly consistent slow-wind plasma regime across heliocentric distances.

Table 1
Solar Orbiter Intervals Used in This Study

Start Time	End Time
2020-07-17 00:00:00	2020-07-17 16:00:00
2022-03-20 04:30:00	2022-03-20 16:30:00
2022-03-27 00:00:00	2022-03-27 16:00:00
2022-04-06 04:30:00	2022-04-06 18:30:00
2022-04-07 00:00:00	2022-04-07 23:00:00
2023-04-02 16:30:00	2023-04-03 02:30:00
2024-10-01 00:00:00	2024-10-01 16:30:00
2024-10-06 04:00:00	2024-10-07 23:30:00
2024-10-08 04:00:00	2024-10-09 12:30:00
2025-04-09 15:30:00	2025-04-10 23:00:00
2025-09-12 00:00:00	2025-09-12 23:30:00

2.1. LMD Technique

The mode decomposition method identifies the admissible modes in an MHD plasma from a set of plasma and magnetic

Table 2
Summary of the Fluctuation Components in the Mode Decomposition Solution Vector $\boldsymbol{x}$

Component	Variables
Entropy mode	$\delta\rho^{e}$
Fast MS mode	$\delta p^{f\pm}$, $\delta\hat{u}_{x,y}^{f\pm}$, $\delta\hat{u}_{z}^{f\pm}$, $\delta\hat{B}_{x,y}^{f\pm}$, $\delta\hat{B}_{z}^{f\pm}$
Slow MS mode	$\delta p^{s\pm}$, $\delta\hat{u}_{x,y}^{s\pm}$, $\delta\hat{u}_{z}^{s\pm}$, $\delta\hat{B}_{x,y}^{s\pm}$, $\delta\hat{B}_{z}^{s\pm}$
Alfvén mode	$\delta\hat{u}_{x,y}^{A\pm}$, $\delta\hat{u}_{z}^{A\pm}$, $\delta\hat{B}_{x,y}^{A\pm}$, $\delta\hat{B}_{z}^{A\pm}$, $\phi^{A\pm}$
Magnetic island	$\delta\hat{B}_{x,y}^{i\pm}$, ϕ^{i}

Note. The superscripts + and − denote forward and backward propagation with respect to the background magnetic field $\boldsymbol{B}_0$, respectively.

field fluctuations measured by a single spacecraft at a specific frequency and an inferred wavenumber $\boldsymbol{k}_m$. This method was developed by G. Zank et al. (2023) and has been successfully applied to a range of solar wind intervals, including shock transition regions, radial alignment intervals, sub-Alfvénic solar wind intervals, and different solar wind regimes, to separate observed fluctuations into their constituent plasma modes. To apply the LMD technique, we first transform the RTN measurements into a mean-field coordinate system, with $\boldsymbol{B}_0$ aligned along $\hat{z}$ and $\boldsymbol{U}_0$ confined to the x–z plane. For each interval, a uniform background state, (ρ_0, p_0, $\boldsymbol{v}_0$, $\boldsymbol{B}_0$), is defined from the time-averaged plasma and magnetic field measurements. The observed fluctuations relative to this background, $\delta\boldsymbol{\Psi}_m(t) = [\delta\rho_m(t), \delta p_m(t), \delta\boldsymbol{v}_m(t), \delta\boldsymbol{B}_m(t)]$, are then decomposed into properly polarized linear MHD modes—forward/backward Alfvén, forward/backward fast and slow MS, entropy, and magnetic island—by combining the linear MHD eigenrelations with phase constraints derived from the Doppler-shifted frequencies and inferred wavevector direction. The direction of the associated wavevector, $\boldsymbol{k}_m$, is estimated from the magnetic field measurements over each interval using minimum variance analysis (B. U. Sonnerup 1998), subject to the consistency condition $\boldsymbol{k}_m \cdot \delta\hat{\boldsymbol{B}}_m = 0$. This leads to a linear system, $\boldsymbol{Ax} = \boldsymbol{b}$, in which the measured plasma and magnetic field fluctuations are related to the amplitudes of the individual linear modes. Here, $\boldsymbol{b}$ represents the observed fluctuation vector, while $\boldsymbol{x}$ contains the unknown mode amplitudes to be determined. Solving this system allows the measured fluctuations to be decomposed into entropy, fast MS, slow MS, Alfvén, and magnetic island components as shown in Table 2. To ensure a physically consistent decomposition, only intervals for which the reconstructed solution satisfies $\boldsymbol{x} \leqslant 1$ are retained for further analysis; intervals exceeding this threshold indicate a poor fit between the decomposed modes and the observed fluctuations and are therefore discarded.

The detailed construction of the amplitude matrix, the associated phase relations, and the numerical implementation of the decomposition algorithm are described in G. Zank et al. (2023), G. P. Zank et al. (2024), and S. P. Gautam et al. (2025). After obtaining the mode-separated fluctuations, we compute their power spectral densities (PSDs) to examine how the fluctuation power of each linear mode is distributed over the spacecraft-frame frequency. We further evaluate the mean fluctuation energy and relative power fraction of each mode for the selected intervals, enabling us to quantify their variation with heliocentric distance.

3. Analysis

3.1. Radial Evolution of Solar Wind Parameters

We first examine the broad radial trends seen in the solar wind environment as shown in Figure 1. The data from all selected intervals are combined and sorted into heliocentric distance bins of width 5 $R_\odot$. Here, the sound speed, $C_s = \sqrt{\frac{\gamma P}{\rho}}$, where P is the thermal pressure and $\rho \simeq N_p m_p$ is the proton mass density, characterizes the pressure restoring force in the plasma and therefore controls the compressive response of the solar wind. The proton plasma beta, β, measures the ratio of thermal to magnetic pressure and indicates whether the plasma dynamics are primarily pressure dominated or magnetically dominated. These quantities are known to be important because the phase speeds, polarizations, and relative energy partition among linear MHD modes depend on C_s, V_A, ρ, and the background magnetic field direction (G. Zank & W. Matthaeus 1992; J. Cho & A. Lazarian 2003; C. C. Chaston et al. 2020). In particular, low-β intervals are expected to be more strongly controlled by magnetic tension and Alfvénic dynamics, whereas higher-β intervals allow thermal pressure and compressive MS fluctuations to play a larger role (G. Zank & W. Matthaeus 1992; J. Cho & A. Lazarian 2003). Thus, variations in these parameters provide the necessary physical context for interpreting changes in the relative contributions of Alfvénic, slow MS, and fast MS fluctuations in each interval.

Panel (a) of Figure 1 shows the radial distribution of the magnetic field magnitude $|B|$. The black curves in all panels are the result of power-law fitting. The magnetic field magnitude decreases approximately as $|B| \propto r^{-2.01}$ with increasing heliocentric distance. This scaling is broadly consistent with the Parker spiral description in the inner heliosphere, where the radial magnetic field component is expected to scale as $B_r \propto r^{-2}$. However, in the full Parker spiral, the azimuthal component scales as $B_\phi \propto r^{-1}$, so the total field magnitude can deviate from a pure r^{-2} law at larger heliocentric distances (E. N. Parker 1958; C. P. Brown et al. 2025). Panel (b) shows the radial distribution of the proton bulk speed V_{sw}, i.e., the solar wind speed, and the sound speed C_s. The red curve in panel (b) is the power-law fit for the sound speed C_s. The solar wind speed and sound speed exhibit power laws of $r^{0.13}$ and $r^{-0.47}$, respectively, reflecting the decrease in plasma temperature with distance from the Sun. Panel (c) displays the proton N_p and electron N_e number densities, which decrease strongly with heliocentric distance, displaying radial profiles of $r^{-1.79}$ and $r^{-1.78}$, respectively. These slopes are close to, but slightly shallower than, the r^{-2} dependence expected for a steady, spherically expanding solar wind with constant radial speed (G. Zank & W. Matthaeus 1992; C. C. Chaston et al. 2020).

Finally, panel (d) shows the plasma beta, β, which generally increases with radial distance as $\sim r^{0.35}$, indicating that the ratio of thermal to magnetic pressure increases farther away from the Sun. Figure 2 illustrates the dependence of compressibility on heliocentric distance r and plasma beta β. Figure 2(a) shows the magnetic compressibility, $C_B = \delta|B|^2/\delta B^2$, as a function of heliocentric distance r, with the color scale representing the solar wind speed. C_B increases toward large r as $C_B \propto r^{0.59\pm0.06}$, reflecting that magnetic field strength fluctuations become progressively larger with increasing distance from the Sun. Figure 2(b) presents the compressibility as a function of plasma beta. It can be seen

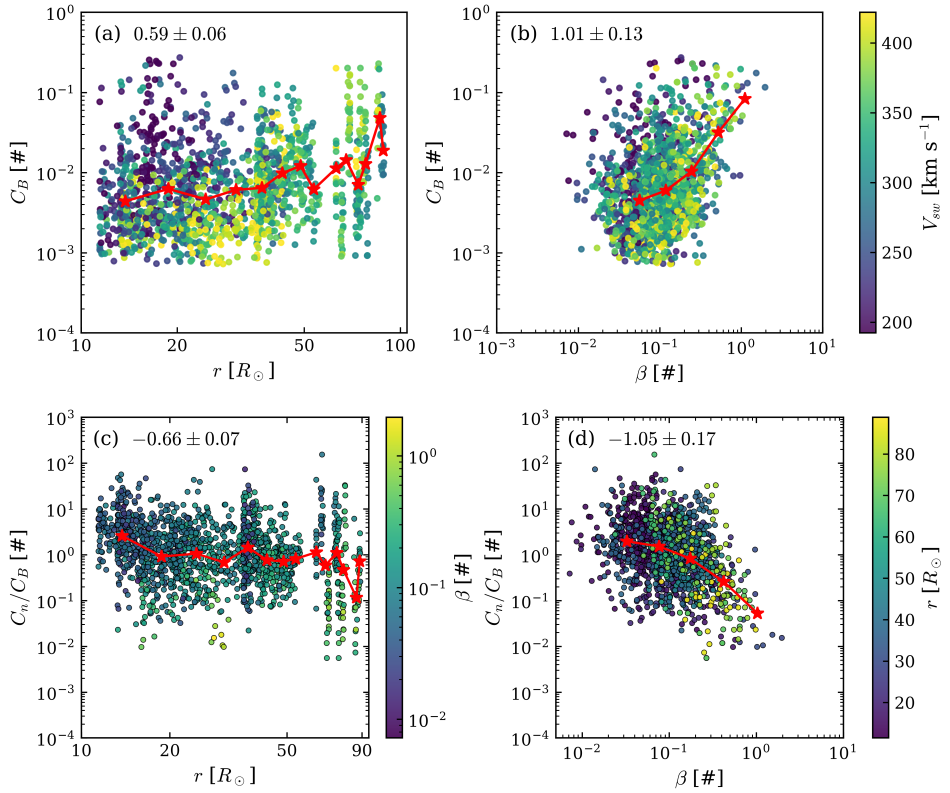


Figure 2. (a) Magnetic compressibility C_B as a function of heliocentric distance r. (b) C_B as a function of plasma beta β colored by solar wind speed $V_{\rm sw}$. (c) Ratio of C_n/C_B as a function of r, colored by β. (d) Ratio of C_n/C_B as a function of β, colored by r. The red dots with fitted lines represent averaged mean values using radial bins of 6 $R_\odot$.

that the periods of solar wind $V_{\rm sw} > 350\,{\rm km\,s^{-1}}$ have a lower compressibility, consistent with previous observations (C.-Y. Tu & E. Marsch 1995; R. Bruno & V. Carbone 2013), and overall, the data can be fit to a power law, $C_B \propto \beta^{1.01\pm0.13}$. This indicates that more compressive magnetic fluctuations are favored in higher-β intervals.

Figures 2(c) and (d) show the ratio of C_n/C_B where $C_n = \delta n^2/\langle n\rangle^2 = {\rm Var}(n)/\langle n\rangle^2$, as a function of r and β, respectively. The dependence of C_n/C_B on r as $C_n/C_B \propto r^{-0.66\pm0.07}$ and on β as $C_n/C_B \propto \beta^{-1.05\pm0.17}$ decreases with both distance and plasma beta. This reflects that density compressibility is relatively more important in the near-Sun, low-β wind, while magnetic compressibility becomes progressively more important at larger r and higher β.

3.2. Turbulent Mode Analysis

In this study, we select 133 30 minute intervals spanning heliocentric distances from 32 to 90 $R_\odot$, combining observations from PSP and Solar Orbiter. Using this event set, we investigate PSDs, the radial evolution of the turbulent modes' energy, variance anisotropy, mode power fractions, and the magnetic field fluctuations' spectral index.

3.2.1. Power Spectral Densities Measured by Parker Solar Probe

Figure 3 presents the spectral properties of decomposed density, velocity, and magnetic fluctuations as a function of frequency measured by PSP. The bold curves represent the mean PSDs of the selected intervals, whereas the faint blurred curves in the background show the spectra from all individual intervals. The left panels (a) and (d) in Figure 3 represent the density fluctuations contributed by the various modes: the entropy ($\delta\rho^e$) mode, the forward and backward fast MS modes ($\delta\rho^{f\pm}$), and the forward and backward slow MS modes ($\delta\rho^{s\pm}$). In the frequency density spectra, the forward/backward fast MS modes appear to carry the largest power, while the entropy mode is generally smaller and the forward/backward slow MS modes' contribution is the weakest. The entropy mode possesses a flatter spectrum, reflecting a saturation of fluctuations in which the Fourier mode amplitudes approach a limiting value (R. Bruno et al. 2019). This result differs from many previous solar wind studies, especially near 1 au, which have found that compressive fluctuations are dominated by slow mode–like or pressure-balanced structures (C.-Y. Tu & E. Marsch 1995; G. Howes et al. 2012).

The middle panels (b) and (e) of Figure 3 illustrate velocity fluctuations consisting of the components of forward and backward fast ($\delta U^{f\pm}$) and slow ($\delta U^{s\pm}$) MS modes and transverse forward and backward Alfvénic ($\delta u^{A\pm}$) modes. In the velocity fluctuation panels, the Alfvénic components are the dominant contributors across most frequencies, while the fast modes are slightly weaker than the transverse incompressible modes and the slow modes are significantly the smallest. The overall large contributions to the velocity fluctuations are primarily attributed to the backward-propagating Alfvénic fluctuations. This behavior is consistent with the well-established picture that solar wind turbulence is primarily Alfvénic, especially in the inner heliosphere (R. Bruno & V. Carbone 2013). The comparatively weak slow-mode velocity power in MHD turbulence is often described as being passively mixed by the Alfvénic cascade

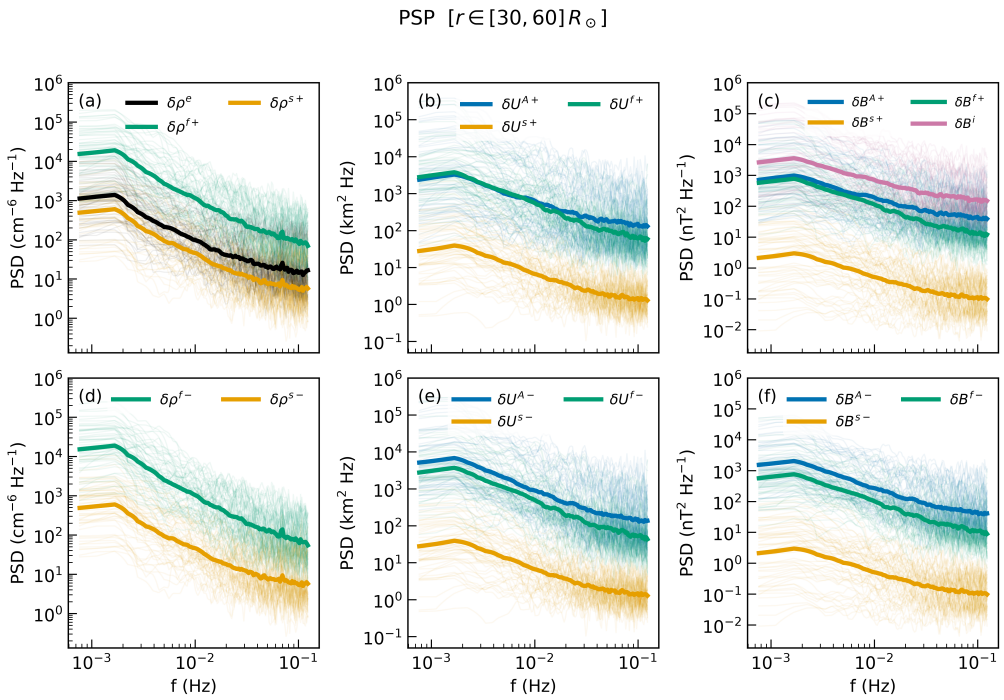


Figure 3. PSDs for (a), (d) density fluctuations, consisting of entropy (black curve), fast MS (green curve), and slow MS (orange curve) modes; (b), (e) velocity field fluctuations, consisting of Alfvén (blue curve), fast MS (green curve), and slow MS (orange curve) modes; and (c), (f) magnetic field fluctuations, consisting of magnetic island (purple curve), Alfvén (blue curve), fast MS (green curve), and slow MS (orange curve) modes measured by PSP.

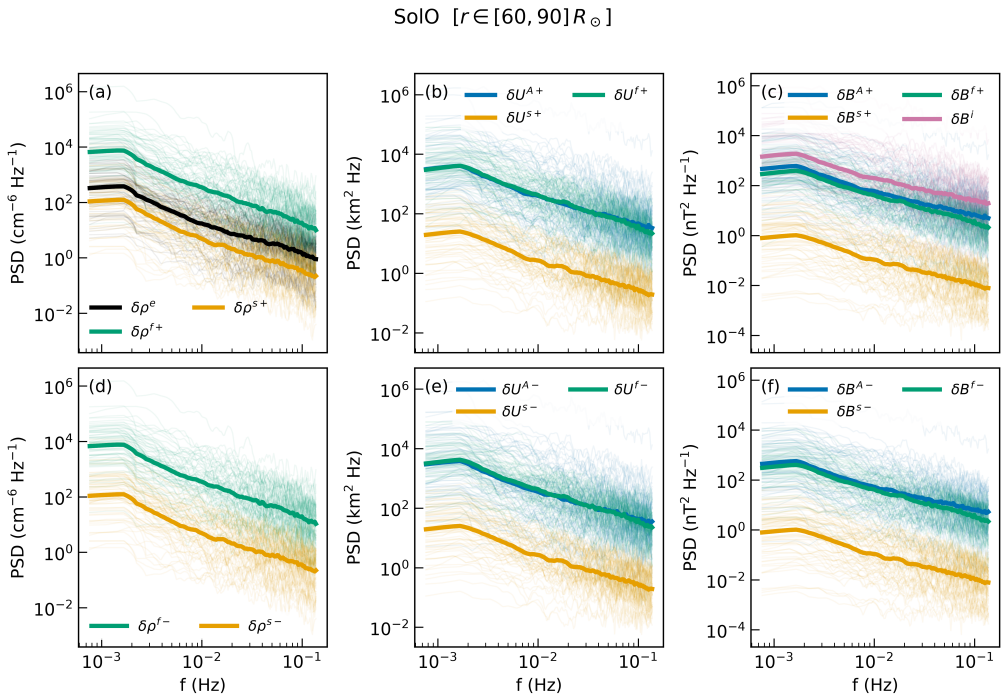


Figure 4. PSDs of density, velocity, and magnetic field fluctuations across selected intervals, in the same format as Figure 3, as measured by Solar Orbiter.

rather than independently dominating it. The right panels (c) and (f) in Figure 3 display the magnetic field fluctuations as a function of frequency for the components of magnetic islands (δB^i), forward and backward fast ($\delta B^{f\pm}$) and slow ($\delta B^{s\pm}$) MS modes, and transverse forward and backward Alfvénic ($\delta B^{A\pm}$) modes. In the magnetic fluctuation panels, the dominant contribution is carried by the magnetic island mode, followed by Alfvénic fluctuations, whereas the fast and especially the slow MS contributions remain much smaller. This might suggest that the magnetic field fluctuations are also controlled by a substantial quasi-2D component or coherent structures, including current sheets, flux rope–like structures, and magnetic islands (G. Zank et al. 2023).

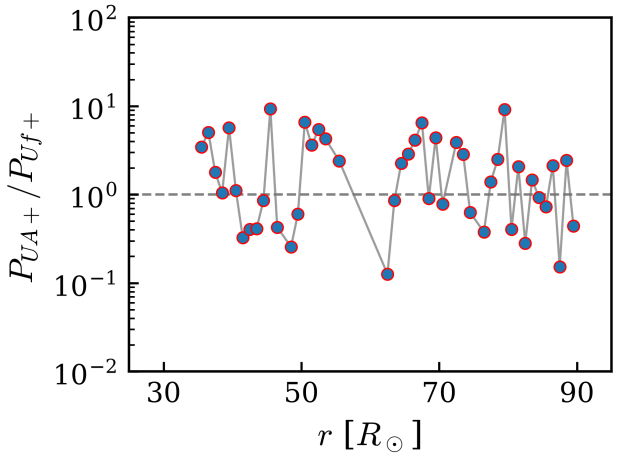


Figure 5. Ratio of the power in velocity field fluctuations between forward Alfvén and fast MS modes as a function of heliocentric distance.

3.2.2. Power Spectral Densities Measured by Solar Orbiter

Figure 4 presents the spectral properties of the decomposed density, velocity, and magnetic fluctuations as a function of frequency measured by Solar Orbiter, following the same format as Figure 3 for PSP. For the density fluctuations, the entropy ($\delta\rho^e$), fast ($\delta\rho^{f\pm}$), and slow ($\delta\rho^{s\pm}$) modes show spectral trends identical to those observed by PSP. However, the overall amplitudes are consistently lower in the SolO measurements compared to PSP. The middle panels (b) and (e) represent the velocity fluctuations, where the Alfvénic ($\delta U^{A\pm}$) and fast MS ($\delta U^{f\pm}$) modes exhibit comparable mean PSD amplitudes in the observed slow solar wind measured by SolO, while the slow MS modes ($\delta U^{s\pm}$) remain distinctly weaker. For the magnetic fluctuations, the right panels (c) and (f) show dominant contributions from the magnetic island and Alfvénic components, with fast and slow modes remaining subdominant. The spectral behavior and relative ordering of modes are consistent between PSP and SolO, although the SolO spectra exhibit lower power across all frequencies.

Since the velocity fluctuation PSDs of the forward Alfvénic and fast MS modes are of comparable magnitude in both the PSP and SolO measurements, we examine their power ratio, P_{UA^+}/P_{Uf^+}, as a function of heliocentric distance in order to assess their relative contributions. Figure 5 examines the ratio between P_{UA^+}/P_{Uf^+}. It shows that the ratio fluctuates around unity, but is greater than 1 for most intervals, indicating that forward Alfvénic modes generally contribute slightly more than forward fast modes over the selected heliocentric distance $r \in [32, 90]\, R_\odot$.

3.2.3. Radial Evolution of Fluctuating Energies

Figure 6 plots the radial evolution of the mean turbulent energies for velocity field fluctuations, magnetic field fluctuations, and density fluctuations across the selected 133 30 minute intervals. The radial profiles of the observed modes are summarized in Table 3. Panels (a) and (b) show the mean turbulent energies for velocity field fluctuations, consisting of the forward and backward Alfvén ($\delta U^{A\pm}$, blue) modes, forward and backward fast MS ($\delta U^{f\pm}$, green) modes, and forward and backward slow MS ($\delta U^{s\pm}$, orange) modes, with heliocentric distance. In the figure, the Alfvénic modes clearly dominate the velocity fluctuation energy, with both forward (δU^{A+}) and backward (δU^{A-}) components remaining slightly larger than the fast and slow MS contributions across all distances. The forward and backward Alfvénic modes exhibit a relatively shallow decay with heliocentric distance, following comparable power-law scalings of approximately $r^{-0.27}$ and $r^{-0.45}$, respectively. In contrast, the energy of forward fast (δU^{f+}) MS modes shows a slight decline ($\sim r^{-0.30}$), whereas the backward fast (δU^{f-}) MS mode shows a very weak decay ($\sim r^{-0.07}$) with distance. The forward and backward slow ($\delta U^{s\pm}$) modes' contribution remains the weakest and decreases most rapidly ($\sim r^{-1.49}$) with distance, indicating that compressive velocity fluctuations become subdominant relative to the Alfvénic component.

The middle panels (c) and (d) of Figure 6 plot the radial evolution of the magnetic variance for forward Alfvén (δB^{A+}) modes, fast (δB^{f+}) and slow (δB^{s+}) MS modes, and magnetic island (δB^{i}) modes (left) as well as the corresponding backward modes (right) in the solar wind as a function of the heliocentric distance. In the figure, the magnetic island mode appears as a dominant contributor with significant energy and follows a power law of $r^{-1.90}$. The mean turbulent energies for the forward Alfvén (δB^{A+}) mode and fast (δB^{f+}) and slow (δB^{s+}) MS modes decrease approximately as $r^{-1.96}$, $r^{-1.78}$, and $r^{-2.96}$ with increasing heliocentric distance. Panel (d) shows that the backward Alfvén (δB^{A-}) mode and fast (δB^{f-}) and slow (δB^{s-}) MS modes in the slow solar wind are relatively higher than the corresponding forward modes (panel (c)). The backward Alfvén (δB^{A-}) mode remains the dominant contributor and follows a comparable radial decay, approximately as $r^{-2.17}$. The backward fast (δB^{f-}) mode is weaker and scales approximately as $r^{-1.55}$, while the slow (δB^{s-}) mode again shows the steepest decline, scaling as $r^{-2.96}$. This consistent ordering indicates that, even in the magnetic field, incompressible fluctuations dominate compressive modes throughout the entire radial range.

Panels (e) and (f) show the radial evolution of entropy ($\delta\rho^e$) modes and forward fast ($\delta\rho^{f+}$) and slow ($\delta\rho^{s+}$) MS modes (left) as well as the corresponding backward modes (right) for the variance of the density fluctuations in the solar wind as a function of the heliocentric distance. Panel (e) shows that the forward fast-mode contribution is the largest and shows a strong decay $r^{-2.08}$, indicating that fast-mode compressibility persists over a broad radial range. The forward slow-mode contribution is smaller and decreases more steeply, $r^{-4.12}$. The entropy mode (black) lies in between, with a significant decay of roughly $r^{-3.70}$, indicating that nonpropagating density structures also diminish significantly with radial expansion. The bottom panel (f) shows that the backward fast ($\delta\rho^{f-}$) and slow ($\delta\rho^{s-}$) MS modes in the slow solar wind are relatively higher than the corresponding forward modes (panel (e)). The backward fast ($\delta\rho^{f-}$) mode dominates the density fluctuations and shows a relatively shallow radial decay of $r^{-1.77}$. The slow modes contribute only a minor fraction to density fluctuations at larger heliocentric distances.

We compute the variance anisotropy of the magnetic island (δB^{i}) mode and Alfvén ($\delta B^{A\pm}$) modes from the overall collected spectra. The magnetic variance anisotropy is defined as $\frac{\langle \delta B^{i^2} \rangle}{\langle \delta B^{A^2} \rangle}$, where $\delta B^{A} = \sqrt{\delta B^{A^{+2}} + \delta B^{A^{-2}}}$. Figure 7 indicates a weak but systematic increase of $\langle \delta B^{i^2} \rangle / \langle \delta B^{A^2} \rangle$ with heliocentric distance, suggesting that the transverse incompressible turbulence becomes progressively more dominated by the magnetic island component relative to the Alfvénic component as the solar wind evolves outward. In this regard, despite the broad

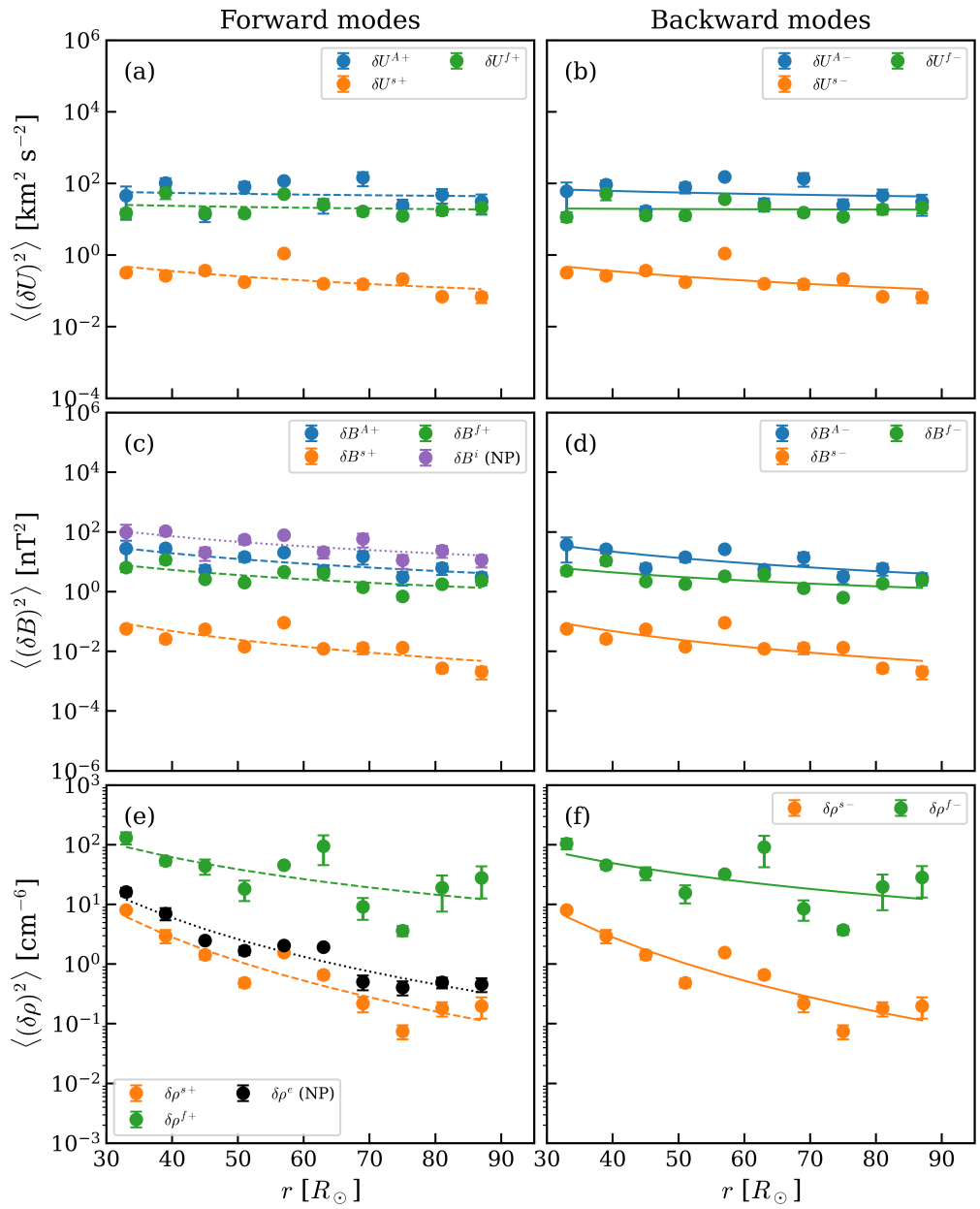


Figure 6. Mean energies of the velocity, magnetic field, and density fluctuations over the selected 30 minute intervals as a function of heliocentric distance. Top panels (a) and (b): velocity field fluctuations, comprising forward Alfvén (blue), fast MS (green), and slow MS (orange) modes and backward Alfvén (blue), fast MS (green), and slow MS (orange) modes. Middle panels (c) and (d): magnetic field fluctuations, consisting of island modes (purple), forward Alfvén (blue) and fast (green) / slow (orange) MS modes, and backward Alfvén (blue) and fast (green) / slow (orange) MS modes. Bottom panels (e) and (f): density fluctuations, consisting of entropy (black), forward fast (green) and slow (orange) MS modes, and backward fast (green) and slow (orange) MS modes. NP represents the nonpropagating modes. The radial profiles are constructed by binning the data in heliocentric distance using bins of width 5 $R_\odot$. For each radial bin, the plotted value corresponds to the mean of the quantity within that bin, and the associated error bar represents the standard error of the mean calculated from all measurements in the same radial interval.

range of values observed at nearly all radial distances, the weak outward increase of the ratio from ∼2.5 to ∼5, with a radial exponent of 0.13, may reflect the gradual enhancement, or survival, of nonpropagating transverse structures in the expanding solar wind.

3.2.4. Radial Distribution of the Modal Contribution to Energy

We examine the fractional contribution of different linear MHD modes to the total fluctuation energy across heliocentric distance. For each radial bin, the fractional power of mode m is calculated as $f_m(r_i) = P_m(r_i)/\sum_k P_k(r_i) \times 100\%$, where $P_m(r_i)$ denotes the power of mode m in the ith radial bin, and $\sum_k P_k(r_i)$ is the total power summed over all relevant modes of the same fluctuation field within that bin. Therefore, the modal fractions are calculated independently within each radial interval, and are shown as a function of r in Figure 8. Panels (a) and (b) show the fractional power of the velocity fluctuations for the forward Alfvén (δU^{A+}), forward fast (δU^{f+}) MS, and forward slow (δU^{s+}) MS modes, and the backward Alfvén (δU^{A-}), backward slow (δU^{s-}) MS, and backward fast (δU^{f-}) MS modes. For the velocity fluctuations, the power is partitioned

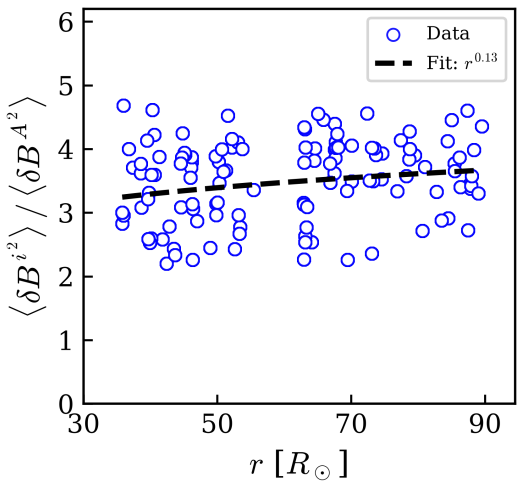


Figure 7. Scatter plot of computed magnetic variance anisotropy versus r. The black line denotes the power-law fit.

Table 3
Radial Power-law Exponents of the Decomposed Fluctuation Modes

Mode	Velocity, δU	Magnetic Field, δB	Density, $\delta\rho$
A^+	−0.27	−1.96	⋯
A^-	−0.45	−2.17	⋯
s^+	−1.49	−2.96	−4.12
s^-	−1.49	−2.96	−4.12
f^+	−0.30	−1.78	−2.08
f^-	−0.07	−1.55	−1.77
e	⋯	⋯	−3.70
i	⋯	−1.90	⋯

Note. Each quantity is fitted as $\langle (\delta X)^2 \rangle \propto r^\alpha$.

mainly between the forward/backward Alfvén and fast modes, and their relative contributions vary with heliocentric distance. The Alfvén modes remain important throughout, but the forward/backward fast modes also contribute substantially and are comparable in several radial bins. In contrast, the forward/backward slow modes remain consistently subdominant over the heliocentric distance ∼32–90 $R_\odot$.

Panels (c) and (d) of Figure 8 show the fractional power of the magnetic field fluctuations, comprising the magnetic island (δB^i), forward Alfvén (δB^{A+}), forward fast MS (δB^{f+}), and forward slow MS (δB^{s+}) modes in the left panel, and the backward Alfvén (δB^{A-}), backward fast MS (δB^{f-}), and backward slow MS (δB^{s-}) modes in the right panel. The magnetic fluctuations are dominated primarily by the magnetic island (δB^i) modes, which remain the largest contributor over the full radial range, while the forward Alfvén and fast MS modes provide secondary but still significant contributions that vary with heliocentric distance. Panel (d) displays the radial variation of the fractional power contained in the backward magnetic fluctuations. The backward Alfvénic component, δB^{A-}, remains the dominant contributor over most of the radial range considered. In addition, the backward fast MS component also carries a substantial fraction of the magnetic fluctuation power across several radial bins, indicating that both modes make important contributions to the backward-propagating magnetic fluctuations. Conversely, the slow MS modes remain weaker in both the forward- and backward-propagating components.

Panels (e) and (f) of Figure 8 show the fractional power of density fluctuations, comprising the entropy ($\delta\rho^e$), forward fast MS ($\delta\rho^{f+}$), and forward slow MS ($\delta\rho^{s+}$) modes in the left panel, and the backward fast MS ($\delta\rho^{f-}$) and backward slow MS ($\delta\rho^{s-}$) modes in the right panel. The density fluctuations are dominated primarily by the forward and backward fast MS modes, which contribute the largest fraction of the power over most of the radial range ∼32–90 $R_\odot$. The entropy mode provides the next most important contribution, while the slow MS modes remain less significant in both forward- and backward-propagating components.

3.2.5. Radial Scaling of the Fluctuation PSDs

A key diagnostic used to characterize the nature of the turbulent cascade is the power-law spectral index α, obtained from the magnetic and entropy fluctuation frequency power spectrum, $E \propto f^\alpha$. For each interval, α was determined by fitting the magnetic spectrum over the frequency range 6×10^{-3} Hz $< f_{sc} < 6 \times 10^{-2}$ Hz, and the resulting values are shown as a function of radial distance in Figure 9. Each panel shows the spectral index α as a function of heliocentric distance r, with individual interval measurements (red points), bin-averaged values (black points), and corresponding power-law fits (dashed lines).

Panels (a) and (b) of Figure 9 show that the Alfvénic fluctuations ($\delta B^{A\pm}$) exhibit relatively shallow spectral indices ($\alpha \gtrsim -3/2$), occasionally approaching $\alpha \sim -1$ closer to the Sun, with only a weak radial dependence. This behavior is consistent with the dominance of outward-propagating Alfvénic turbulence in the solar wind and agrees with previous observations that report relatively shallow spectra for Alfvénic components closer to the Sun (C. H. K. Chen et al. 2020).

The second row of panels (c) and (d) shows the slow MS components. The forward slow mode (δB^{s+}) exhibits a systematically steeper spectrum, with α approaching values closer to −1.1 to −1.3, and a mild trend of steepening with increasing r. Similarly, the backward slow mode (δB^{s-}) follows a comparable trend. This is qualitatively consistent with the compressive character of slow-mode fluctuations, which are commonly associated with the compressive component of inertial-range solar wind turbulence and may display steeper spectra than the dominant Alfvénic component (G. Howes et al. 2012; D. Verscharen et al. 2017).

The third row of panels (e) and (f) in Figure 9 presents the fast MS components. Both forward (δB^{f+}) and backward (δB^{f-}) fast modes display relatively shallow spectral indices, typically around $\alpha \sim -1$, with minimal radial variation. This could suggest that fast modes contribute across a broad range of scales without undergoing strong scale-dependent steepening, consistent with previous studies indicating that fast modes are less anisotropic and may exhibit flatter spectra compared to Alfvénic turbulence (J. Cho & A. Lazarian 2003; H. Yan & A. Lazarian 2004). The bottom panel (g) in Figure 9 shows the entropy mode ($\delta\rho^e$), which exhibits spectral indices $\alpha \lesssim -1.3$ and noticeable scatter. This is consistent with the interpretation of entropy fluctuations as advected, nonpropagating structures that undergo passive scalar cascade and dissipation (G. Zank et al. 2020). Finally, panel (h) represents the magnetic island (δB^i) or coherent structure contributions, showing moderately steep spectral indices with significant variability. The presence

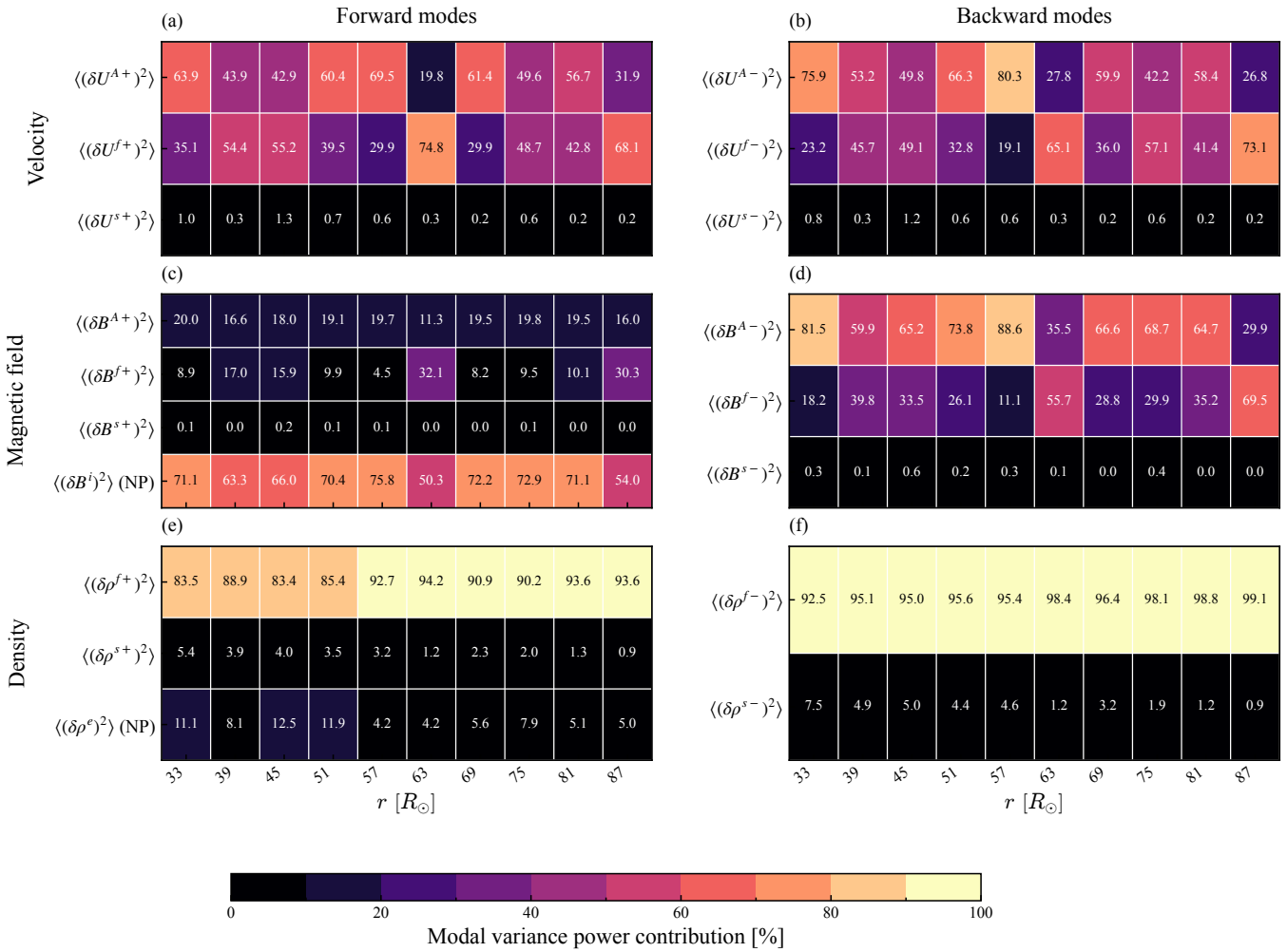


Figure 8. Radial variation of the fractional modal variance power contribution for the velocity, magnetic field, and density fluctuations over the selected intervals. The horizontal axis gives the mean heliocentric distance of each radial bin, and the color scale denotes the modal variance power contribution in percent.

of such structures is consistent with the picture of solar wind turbulence as a mixture of propagating waves and coherent, quasi-2D structures such as flux ropes and current sheets (G. Zank et al. 1996). A detailed summary of the mean spectral indices of the magnetic mode and entropy fluctuations along with their uncertainty is presented in Table 4.

4. Discussion

In this work, we have used PSP and SolO observations over the heliocentric distance $r \sim 32$–$90\,R_\odot$ to study the radial evolution of turbulent fluctuations in the inner heliosphere using the LMD technique. In the first part of this paper, we showed trends in the radial evolution of solar wind parameters as the solar wind expands over $r \sim 11$–$90\,R_\odot$. Our analysis shows that the large-scale solar wind environment evolves with heliocentric distance, indicating a transition from a strongly magnetized, low-β plasma near the Sun to a more weakly magnetized, higher-β, and super-Alfvénic flow farther out. This evolution sets the background conditions that regulate the nature of turbulent fluctuations, including their compressibility, mode composition, and cascade dynamics. Consistent with this evolution, the magnetic compressibility increases with both heliocentric distance and plasma beta ($C_B \propto r^{0.59\pm0.06}$, $C_B \propto \beta^{1.01\pm0.13}$), while the relative importance of density fluctuations becomes progressively weaker relative to magnetic fluctuations ($C_n/C_B \propto r^{-0.66\pm0.07}$, $C_n/C_B \propto \beta^{-1.05\pm0.17}$). This indicates that compressive turbulence becomes increasingly dominated by magnetic field variations, reflecting the changing nature of compressible turbulence in the expanding solar wind (R. Bruno & B. Bavassano 1993; R. Bruno et al. 2006), which may have implications for the radial evolution of other turbulent characteristics.

To identify how linear MHD modes evolve with heliocentric distance, we examined the radial evolution of the decomposed modes with respect to the variance of density, velocity, and magnetic field fluctuations. We extended the mode decomposition study of G. Zank et al. (2023) and M. Karki et al. (2025), which examined the modal composition of turbulent fluctuations at 1 au, by applying the same framework over a broad radial range in the inner heliosphere. To quantify the fluctuation amplitudes, we first calculated the PSDs of each decomposed fluctuating field and then integrated the PSDs over the frequency range $6 \times 10^{-3}\,\mathrm{Hz} < f_{sc} < 6 \times 10^{-2}\,\mathrm{Hz}$ to obtain the corresponding variances.

We also computed the variance anisotropy based on the decomposed transverse incompressible components of magnetic Alfvén modes $\delta B^{A\pm}$ and magnetic island modes δB^{i} using collected spectra to determine the radial distribution of the relative modal power. The observed increase of $\langle \delta B^{i^2} \rangle / \langle \delta B^{A^2} \rangle$ with heliocentric distance suggests that transverse

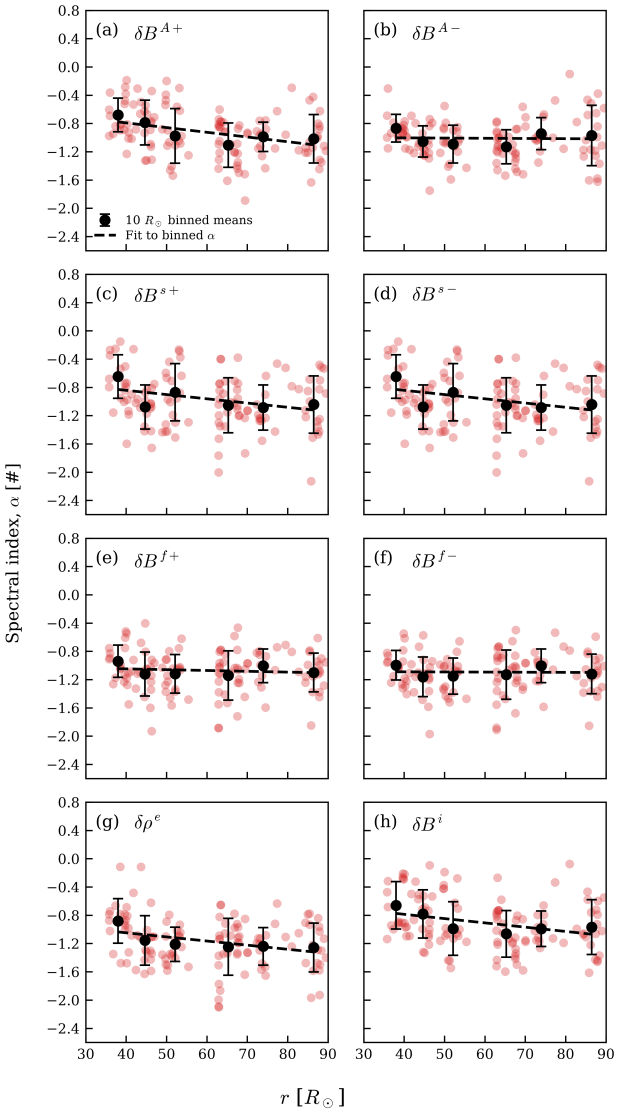


Figure 9. Variation of the spectral index of the frequency PSD of the magnetic field (δB) fluctuations and density entropy ($\delta\rho^e$) fluctuations with heliocentric distance, r, in the MHD inertial range (6×10^{-3} Hz $< f_{sc} < 6 \times 10^{-2}$ Hz). The red dots represent the spectral measurements, and the black line denotes the fit obtained using radial bins of width 10 $R_\odot$.

Table 4
Summary of the Mean Spectral Indices of the Magnetic Mode and Entropy Fluctuations

Panel	Mode	$\langle\alpha\rangle \pm \sigma_\alpha$
(a)	δB^{A+}	-0.93 ± 0.16
(b)	δB^{A-}	-1.01 ± 0.10
(c)	δB^{s+}	-1.14 ± 0.17
(d)	δB^{s-}	-1.14 ± 0.17
(e)	δB^{f+}	-0.90 ± 0.08
(f)	δB^{f-}	-0.97 ± 0.07
(g)	$\delta \rho^{e}$	-1.17 ± 0.14
(h)	δB^{i}	-0.91 ± 0.15

Note. The quoted uncertainty represents the standard deviation of the binned mean spectral index values.

incompressible turbulence becomes progressively more dominated by magnetic island or quasi-2D structure–like fluctuations than by Alfvénic fluctuations. This trend implies that nonpropagating coherent magnetic structures remain significant (G. Zank & W. Matthaeus 1992; G. P. Zank & W. Matthaeus 1993; J. W. Bieber et al. 1996; J. Saur & J. W. Bieber 1999; P. Hunana & G. Zank 2010; L.-L. Zhao et al. 2023) as the solar wind expands outward. Presumably, this would indicate a gradual increase in intermittency with increasing heliocentric distance. We also calculated the fractional contribution of different linear MHD modes with respect to their total fluctuation energy across heliocentric distance. The dominance of Alfvénic and fast MS modes in velocity fluctuations, with spectral indices between ~ -0.8 and -1.4, is consistent with the nearly incompressible MHD framework (G. Zank & W. Matthaeus 1992; G. P. Zank & W. Matthaeus 1993; G. P. Zank et al. 2017), in which Alfvénic fluctuations drive the dominant turbulent energy cascade while fast modes contribute to compressive energy transfer (J. Cho & A. Lazarian 2003; G. Howes et al. 2012). The weak slow-mode contribution and the lack of significant radial variation in the spectral indices suggest that the inertial-range cascade structure is largely preserved as the solar wind expands, with Alfvénic turbulence remaining the primary channel for cross-scale energy transfer and consequently plasma heating (R. Bruno & V. Carbone 2013; C. H. K. Chen et al. 2020). The dominance of magnetic island structures in magnetic fluctuation power reflects the significant quasi-2D component of solar wind turbulence, which may arise from the nonlinear steepening and interaction of Alfvénic fluctuations that generate coherent, nonpropagating magnetic structures such as flux tubes and current sheets (G. Zank & W. Matthaeus 1992; G. P. Zank & W. Matthaeus 1993; W. H. Matthaeus et al. 1996). These quasi-2D structures are particularly important because they provide the dominant contribution to the perpendicular turbulent energy cascade (J. V. Shebalin et al. 1983; S. Oughton et al. 1994), and serve as preferred sites for magnetic reconnection, particle acceleration, and plasma heating (P. Dmitruk et al. 2004; J. F. Drake et al. 2006; S. Servidio et al. 2009; G. P. Zank 2014). Their growing dominance over Alfvénic fluctuations with heliocentric distance further suggests that nonlinear dynamics increasingly govern the turbulence evolution as the solar wind expands (R. Bruno & V. Carbone 2013; G. P. Zank et al. 2017; G. Zank et al. 2023).

We found that the density fluctuation power is dominated by fast MS modes, $\langle(\delta\rho^{f\pm})^2\rangle \sim 83\%$–$99\%$, while entropy and slow-mode contributions remain weak. This differs from many solar wind studies that associate compressive inertial-range turbulence mainly with slow mode–like or pressure-balanced fluctuations (C.-Y. Tu & E. Marsch 1995; R. Bruno & V. Carbone 2013); the difference may reflect the sensitivity of the decomposition to the selected intervals, radial range, and local plasma conditions, where transient compressive structures, stream interactions, or near-Sun effects can enhance the fast-mode contribution (S. Banerjee et al. 2016; B. Zieger et al. 2020). The density spectral indices remain broadly similar to the velocity and magnetic field spectra, mostly between ~ -0.8 and -1.4. Different wave modes behave differently in their energy cascade and energy transport properties throughout space. We examined the frequency power-law spectral index α, i.e., $E \propto f^{\alpha}$, obtained from the magnetic and entropy fluctuations to characterize the nature of the turbulent cascade. For each interval, α was determined by fitting the magnetic spectrum over the frequency range 6×10^{-3} Hz $< f_{sc} < 6 \times 10^{-2}$ Hz, and the resulting values are shown as a function of radial distance in Figure 6.

5. Conclusion

Our findings can be summarized as follows.

1. Magnetic compressibility increases with heliocentric distance ($C_B \propto r^{0.59}$), while density fluctuations weaken relative to magnetic fluctuations ($C_n/C_B \propto r^{-0.66}$), indicating that compressive turbulence becomes increasingly dominated by magnetic field variations as the solar wind expands.
2. Velocity fluctuation energy is dominated by the outward Alfvénic component ($\delta U^{\mathrm{A}+} \sim r^{-0.27}$), with the inward component ($\delta U^{\mathrm{A}-} \sim r^{-0.45}$) remaining significant, reflecting the persistence of imbalanced Alfvénic turbulence throughout the inner heliosphere.
3. Magnetic fluctuation energy is carried primarily by transverse nonpropagating magnetic island structures ($\delta B^{i} \sim r^{-1.90}$), with Alfvénic components being secondary ($\delta B^{\mathrm{A}+} \sim r^{-1.96}$, $\delta B^{\mathrm{A}-} \sim r^{-2.17}$), indicating a substantial quasi-2D coherent component is present together with propagating Alfvénic fluctuations.
4. Density fluctuation energy is overwhelmingly dominated by fast MS modes (∼83%–99%), with slow-mode and entropy contributions remaining weak and decaying more steeply with heliocentric distance.
5. The anisotropy ratio $\langle(\delta B^{i})^2\rangle/\langle(\delta B^{\mathrm{A}})^2\rangle$ of incompressible transverse magnetic fluctuations increases with heliocentric distance, suggesting that transverse incompressible turbulence progressively evolves toward quasi-2D magnetic island dominance as the solar wind expands outward.
6. Alfvénic components ($\delta B^{\mathrm{A}\pm}$) exhibit relatively shallow spectra ($\alpha \gtrsim -3/2$), with the forward component occasionally approaching $\alpha \sim -1$ near the Sun and showing only weak radial dependence, consistent with the dominance of outward-propagating Alfvénic turbulence in the inner heliosphere.
7. Slow MS components ($\delta B^{s\pm}$) display systematically steeper spectra ($\alpha \sim -1.2$ to -1.4), expressing a mild steepening trend with increasing heliocentric distance, which reflects their compressive character and distinct cascade behavior relative to the Alfvénic modes.

The limited number of suitable intervals remains a constraint, as the LMD analysis is highly sensitive to data quality and selection criteria, restricting the available events for robust statistical characterization. Future studies using coordinated multispacecraft observations will be essential to extending this analysis beyond the near-Sun slow solar wind regime. In particular, examining larger heliocentric distances and systematically distinguishing between slow and fast solar wind streams will help clarify the evolution of turbulence properties under different source conditions. In the present study, the same thresholds, $\beta < 5$, $1 < M_{\mathrm{A}} < 5$, and $V_{\mathrm{sw}} < 450\,\mathrm{km\,s^{-1}}$, are applied throughout to focus on radial evolution within a consistent slow solar wind regime. Therefore, incorporating variations across different phases of the solar cycle will provide a more complete understanding of how solar activity influences the development of heliospheric turbulence.

Acknowledgments

M.K. and G.P.Z. acknowledge the support of an NSF EPSCoR RII Track-1 Cooperative Agreement OIA-2148653. G.P.Z. acknowledges the partial support of a NASA Parker Solar Probe contract No. SV4-84017. B.L.A. acknowledges Parker Solar Probe and Solar Orbiter funding at GSFC along with NASA grant 80NSSC22K1011. L.A. was partially supported by NASA grant 80NSSC25K7672.

ORCID iDs

Monika Karki https://orcid.org/0000-0001-5356-2267
Gary P. Zank https://orcid.org/0000-0002-4642-6192
B. L. Alterman https://orcid.org/0000-0001-6673-3432
Laxman Adhikari https://orcid.org/0000-0003-1549-5256

References

Adhikari, L., Giri, A., Karki, M., et al. 2025, ApJ, 993, 60
Adhikari, L., Zank, G., Hunana, P., et al. 2017, ApJ, 841, 85
Adhikari, L., Zank, G., Telloni, D., et al. 2024, ApJ, 966, 521
Adhikari, L., Zank, G., Zhao, L.-L., & Webb, G. 2020a, ApJ, 891, 34
Adhikari, L., Zank, G. P., & Zhao, L. 2021, Fluid, 6, 368
Adhikari, L., Zank, G. P., Zhao, L.-L., & Telloni, D. 2022, ApJ, 933, 56
Adhikari, L., Zank, G. P., Zhao, L.-L., et al. 2020b, ApJS, 246, 38
Alterman, B., & D'Amicis, R. 2025, ApJL, 982, L40
Bale, S., Goetz, K., Harvey, P., et al. 2016, SSRv, 204, 49
Balogh, A., Beek, T. J., Forsyth, R., et al. 1992, A&AS, 92, 221
Bandyopadhyay, R., Matthaeus, W. H., McComas, D. J., et al. 2020, ApJS, 246, 48
Banerjee, S., Hadid, L. Z., Sahraoui, F., & Galtier, S. 2016, ApJL, 829, L27
Baruwal, P., Zank, G. P., Adhikari, L., et al. 2026a, ApJ, 998, 9
Baruwal, P., Zank, G. P., Adhikari, L., et al. 2026b, ApJ, 1002, 209
Bieber, J. W., Wanner, W., & Matthaeus, W. H. 1996, JGRA, 101, 2511
Boldyrev, S. 2005, ApJL, 626, L37
Brown, C. P., Maruca, B. A., Prabakaran, V., et al. 2025, GeoRL, 52, e2025GL115186
Bruno, R., & Bavassano, B. 1993, P&SS, 41, 677
Bruno, R., Bavassano, B., D'Amicis, R., Carbone, V., & Sorriso-Valvo, L. 2006, SSRv, 122, 321
Bruno, R., & Carbone, V. 2013, LRSP, 10, 2
Bruno, R., Telloni, D., Sorriso-Valvo, L., et al. 2019, A&A, 627, A96
Case, A. W., Kasper, J. C., Stevens, M. L., et al. 2020, ApJS, 246, 43
Chaston, C. C., Bonnell, J. W., Bale, S. D., et al. 2020, ApJS, 246, 71
Chen, C. 2016, JPlPh, 82, 535820602
Chen, C. H. K., Bale, S. D., Bonnell, J. W., et al. 2020, ApJS, 246, 53
Chen, Y., Hu, Q., & le Roux, J. A. 2019, ApJ, 881, 58
Cho, J., & Lazarian, A. 2003, MNRAS, 345, 325
D'Amicis, R., & Bruno, R. 2015, ApJ, 805, 84
Dmitruk, P., Matthaeus, W. H., & Seenu, N. 2004, ApJ, 617, 667
Drake, J. F., Swisdak, M., Che, H., & Shay, M. A. 2006, Natur, 443, 553
Gautam, S. P., Zank, G. P., Pitňa, A., et al. 2025, ApJ, 989, 82
Glassmeier, K., Motschmann, U., & Stein, R. 1995, AnGeo, 13, 76
Goldreich, P., & Sridhar, S. 1995, ApJ, 438, 763
Horbury, T. S., O'Brien, H., Carrasco Blazquez, I., et al. 2020, A&A, 642, A9
Howes, G., Bale, S., Klein, K., et al. 2012, ApJL, 753, L19
Hunana, P., & Zank, G. 2010, ApJ, 718, 148
Karki, M., Zank, G. P., Adhikari, L., et al. 2025, ApJ, 995, 212
Kasper, J. C., Abiad, R., Austin, G., et al. 2016, SSRv, 204, 131
Lazarian, A., & Cho, J. 2004, Ap&SS, 292, 29
Livi, R., Larson, D. E., Kasper, J. C., et al. 2022, ApJ, 938, 138
Marsch, E., & Tu, C.-Y. 1990, JGRA, 95, 8211
Matthaeus, W. H., Goldstein, M. L., & Roberts, D. A. 1990, JGRA, 95, 20673
Matthaeus, W. H., Zank, G. P., & Oughton, S. 1996, JPlPh, 56, 659
Matthaeus, W. H., Zank, G. P., Oughton, S., Mullan, D. J., & Dmitruk, P. 1999, ApJL, 523, L93
Moldwin, M., Ford, S., Lepping, R., Slavin, J., & Szabo, A. 2000, GeoRL, 27, 57
Oughton, S., Priest, E. R., & Matthaeus, W. H. 1994, JFM, 280, 95
Owen, C. J., Bruno, R., Livi, S., et al. 2020, A&A, 642, A16
Parker, E. N. 1958, ApJ, 128, 664
Saur, J., & Bieber, J. W. 1999, JGRA, 104, 9975

Servidio, S., Matthaeus, W. H., Shay, M. A., Cassak, P. A., & Dmitruk, P. 2009, PhRvL, 102, 115003
Shebalin, J. V., Matthaeus, W. H., & Montgomery, D. 1983, JPlPh, 29, 525
Silwal, A., Zhao, L., Zank, G. P., et al. 2024, ApJ, 972, 168
Silwal, A., Zhao, L., Zhu, X., et al. 2025, ApJS, 278, 40
Sonnerup, B. U. 1998, ISSIR, 1, 185
Telloni, D., Perri, S., Bruno, R., Carbone, V., & D Amicis, R. 2013, ApJ, 776, 3
Telloni, D., Sorriso-Valvo, L., Woodham, L. D., et al. 2021, ApJL, 912, L21
Tu, C.-Y., & Marsch, E. 1994, JGRA, 99, 21481
Tu, C.-Y., & Marsch, E. 1995, SSRv, 73, 1
Verscharen, D., Chen, C. H., & Wicks, R. T. 2017, ApJ, 840, 106
Yan, H., & Lazarian, A. 2004, ApJ, 614, 757
Yao, S., He, J.-S., Marsch, E., et al. 2011, ApJ, 728, 146
Zank, G., Dosch, A., Hunana, P., et al. 2011, ApJ, 745, 35
Zank, G., & Matthaeus, W. 1992, JGR, 97, 17189
Zank, G., Matthaeus, W., & Smith, C. 1996, JGRA, 101, 17093
Zank, G., Nakanotani, M., Zhao, L.-L., Adhikari, L., & Telloni, D. 2020, ApJ, 900, 115
Zank, G., Zhao, L.-L., Adhikari, L., et al. 2021, PhPl, 28, 080501
Zank, G., Zhao, L.-L., Adhikari, L., et al. 2023, ApJS, 268, 18
Zank, G. P. 2014, Transport Processes in Space Physics and Astrophysics, Vol. 877 (Springer)
Zank, G. P., Adhikari, L., Hunana, P., et al. 2017, ApJ, 835, 147
Zank, G. P., Dosch, A., Hunana, P., et al. 2012, ApJ, 745, 35
Zank, G. P., & Matthaeus, W. 1993, PhFl, 5, 257
Zank, G. P., Zhao, L.-L., Adhikari, L., et al. 2024, ApJ, 966, 75
Zhao, L.-L., Zank, G., Hu, Q., et al. 2021, A&A, 650, A12
Zhao, L.-L., Zank, G., Nakanotani, M., & Adhikari, L. 2023, ApJ, 944, 98
Zhao, S., Yan, H., Liu, T. Z., & Hou, C. 2026, ApJ, 996, 46
Zhu, X., He, J., Verscharen, D., Duan, D., & Bale, S. D. 2020, ApJL, 901, L3
Zieger, B., Opher, M., Tóth, G., & Florinski, V. 2020, JGRA, 125, e2020JA028393